



Al-matrix composite based on Al–Ca–Ni–La system additionally reinforced by $L1_2$ type nanoparticles

Torgom K. AKOPYAN, Nikolay A. BELOV, Evgeniya A. NAUMOVA,
Nikolay V. LETYAGIN, Tat'yana A. SVIRIDOVA

National University of Science and Technology MISiS, 4 Leninsky pr., Moscow 119049, Russia

Received 16 August 2019; accepted 20 December 2019

Abstract: The structure of the quaternary Al–(2–4)wt.%Ca–Ni–La system near the aluminum corner has been studied using computational analysis in the Thermo-Calc program and experimental studies (electron microscopy, microprobe analysis and X-ray diffraction). Based on the phase equilibria data obtained, the experimental projection of the liquidus surface and solid state phase-field distribution of the Al–Ca–Ni–La system have been proposed. Microstructure studies reveal that the alloys with the 2–4 wt.% Ca, 2–4 wt.% Ni and 1–3 wt.% La ranges have an ultra-fine hypoeutectic structure with 30% volume fraction of eutectic intermetallics, which allows one to classify these alloys as natural Al-matrix composites. The ultra-fine eutectic structure produces significant strengthening, the magnitude of which can be well described using the modified Orowan looping mechanism model. Small additives of Zr and Sc (0.2 and 0.1 wt.%, respectively) lead to significant strengthening (by ~25%) due to the formation of $L1_2$ type phase ($Al_3(Zr,Sc)$) nanoparticles during annealing of the alloy at 350–400 °C. Due to the high volume fraction of eutectic intermetallics, the new alloys have low coefficients of thermal expansion and high thermal stability of the structure and mechanical properties.

Key words: Al–Ca alloys; eutectic; intermetallics; phase diagram; rare earth element; nanocomposite; microstructure; mechanical properties

1 Introduction

Rare earth metals (RE) are widely used in various industrial fields for the production of structural materials, high corrosion resistant materials, superconductors, high performance magnets, hydrogen storage, etc [1,2]. Moreover, small additives of rare earth elements are used to modify the eutectic of conventional cast aluminum alloys [3–7]. However, technologies of new alloys on the basis of the Al–RE system are actively explored in the aluminum metallurgy [8–14]. Among them, alloys with RE and Ni exhibit the best combination of the strength and the heat resistance [15]. However, due to the high content of Ni and La, these alloys have many disadvantages.

One of them is the high cost of alloys, which is associated with the high cost of Ni and La. Another disadvantage is the high density of alloys due to the high density of Al_3Ni and $Al_{11}La_3$ intermetallic compounds which are in equilibrium with Al.

In our opinion, the transition to the Al–Ca base alloys can help to solve the described disadvantages of the Al–La, Al–Ni and Al–Ni–La alloys. Indeed, calcium is an affordable metal and is widely used in metallurgy. Ca forms a eutectic-type diagram with Al; however, the density of Ca is one of the lowest metals (1.542 g/cm^3). The Al_4Ca phase in the binary eutectic exceeds 30 vol.%, which allows producing Al-matrix composites by simple melting and casting of alloys. Thus, it can be advisable to consider new metal matrix composites based on the Al–Ca eutectic [16–20], additionally containing Ni

and rare-earth element, such as La or Ce. However, the design of Al–Ca–Ni–La base alloys is significantly constrained by the limited information on the quaternary phase diagram. Despite some data can be taken from works dealing with the binary and ternary systems [10,12,13,15,21–24], more complex systems have not been considered in the literature at all. Based on the above, the main purpose of this work is to analyze the structure of the Al–Ca–Ni–La quaternary system near the aluminum corner and evaluate the possibility of designing new aluminum matrix composite alloys based on it.

It should also be noted that, according to Ref. [25], in contrast to branded Al–Si alloys [26], the Al–Ca base alloys can be further strengthened with small additives of zirconium and scandium. In this case, the strengthening is associated with the decomposition of the aluminum solid solution (Al) and simultaneous formation of secondary coherent spherical nanoparticles of L_{12} type phases (Al_3Zr , Al_3Sc or $Al_3(Zr,Sc)$ [27–32]) during simple annealing of the as-cast alloy. In accordance with Ref. [33], to maintain a suitable balance of the alloy cost and maximum strengthening effect, it is advisable to combine alloying with Zr and Sc in amounts of 0.2 and 0.1 wt.%, respectively. Thus, the effect of the small additions on the mechanical properties and microstructure of new alloys is also considered in this work.

2 Experimental

To study the Al₄CaNiLa system, we used seven model alloys presented in Table 1. The alloys were prepared on the basis of 99.99% aluminum in a resistance furnace (GRAFICARBO) with graphite

crucible. Aluminum was placed in the crucible, after its melting, Al–15wt.%Ca and Al–20wt.%Ni binary master alloys were introduced, and after complete melting, lanthanum was introduced at a melt temperature of 730–740 °C. Zirconium and scandium were added using Al–15wt.%Zr and Al–2wt.%Sc master alloys at a melt temperature of 780 °C. After melting of the main components, the melt was held for 5–10 min for obtaining a homogeneous composition, the slag was raked off and the metal was cast into a graphite mold with working cavity dimensions of 10 mm × 20 mm × 180 mm for quaternary alloys and into a metal mold for tensile tests in the case of alloys with Zr and Sc addition. The cooling rate in the molds was about 10 K/s. The casting temperature was 750–820 °C.

Specimen No. 7 was heat treated in muffle electric furnaces with a maintenance temperature error of 3 K. To establish the temperature dependence of (Al) decomposition characteristics during the formation of the L_{12} phase nanoparticles, we performed step-by-step annealing in the range of 250–500 °C with 50 °C step for 3 h exposure (see Table 2) at each stage [23]. After each stage the sample was cooled in air. The stepwise mode allows us to carry out all studies of the influence of heating temperatures on one sample. This method was both informative and economical for the Al alloys.

The microstructure was studied by scanning electron microscopy (SEM, TESCAN VEGA 3) with electron microprobe analysis (EMPA, OXFORD AZtec) and transmission electron microscopy (TEM, JEM–2100). The specimens were prepared by mechanical and electrolytic polishing. The thin foils for TEM were prepared by ion thinning with a PIPS (Precision Ion Polishing System, Gatan) machine and studied at 160 kV.

Table 1 Chemical compositions of experimental alloys

No.	Alloy	Chemical composition/wt.%					
		Al	Ca	Ni	La	Zr	Sc
1	Al ₂ Ca ₄ Ni ₁ La	Bal.	2.0	3.5	1.2	–	–
2	Al ₂ Ca ₃ Ni ₄ La	Bal.	1.9	2.7	3.75	–	–
3	Al ₂ Ca ₂ Ni ₈ La	Bal.	1.9	1.85	7.5	–	–
4	Al ₄ Ca ₃ Ni ₁ La	Bal.	4.0	2.8	1.1	–	–
5	Al ₄ Ca _{2.5} Ni ₃ La	Bal.	4.1	2.2	3.2	–	–
6	Al ₄ Ca _{1.7} Ni ₆ La	Bal.	3.95	1.5	6.1	–	–
7	Al ₄ Ca _{2.5} Ni ₃ La _{0.2} Zr _{0.1} Sc	Bal.	3.8	2.5	2.8	0.22	0.10

Table 2 Annealing modes

Designation	Regime
S250	250 °C, 3 h
S300	S250+300 °C, 3 h
S350	S300+350 °C, 3 h
S400	S350+400 °C, 3 h
S450	S400+450 °C, 3 h
S500	S450+500 °C, 3 h

The Vickers hardness was determined on a DUROLINE MH-6 installation (load of 1 N, and dwell time of 30 s). Room-temperature tension tests were conducted for as-processed bar specimens with a universal testing machine, model Zwick Z250 (the loading rate was 10 mm/min).

X-ray diffraction (XRD) data were collected using Cu K_{α} radiation and treated by software package [34]. The objects of the X-ray diffraction (XRD) study were polished specimens cut from part of the ingots. Based on XRD data, the volume fraction and the periods of the crystal lattice of the phases have been determined. The relative error of a measurement is 10% for the volume fraction and 0.15% for the crystal lattice periods.

Differential scanning calorimetry (DSC) with heating and cooling rates of 10 K/min was performed using a high-temperature DSC Setaram Setsys Evolution (SETARAM Instrumentation, Caluire, France) for ~80 mg specimens. The experiment was carried out in a dynamic Ar atmosphere with a flow rate of 50 mL/min. A temperature accuracy of ± 0.5 °C was obtained.

Dilatometric analysis with a heating rate of 5 K/min was carried out using a quenching dilatometer DIL 805A/D with the possibility of deformation of the sample by compression (TA Instruments, Germany). Dilatometric study was carried out using thermocouples (S-type) in vacuum (~ 0.013 Pa) on cylindrical samples with 6 mm in diameter and 12 mm in length.

To facilitate the preliminary analysis of the quaternary system, a thermodynamic calculation in the Thermo-Calc program and TTAL5 database was initially conducted [35].

3 Results

3.1 Analysis of quaternary Al–Ca–Ni–La system

The TTAL5 database is designed to calculate the phase composition of the multi-component aluminum-based alloys, and contains the thermodynamic values of all the chemical elements of a given quaternary system and the expected phases. Liquidus data of the Al–Ca–Ni–La system at different Ca, Ni and La contents were calculated to define the areas of primary crystallization of phases in equilibrium. The calculated data were verified by analyzing the microstructure of the alloys. The specific type of primary crystals found in the alloys is marked on the calculated diagrams (Fig. 1(a)). In accordance with the obtained calculated data, the aluminum solid solution (Al) can be in equilibrium with three intermetallic compounds, Al_4Ca , Al_3Ni and $Al_{11}La_3$, the main characteristics of which are given in Table 3.

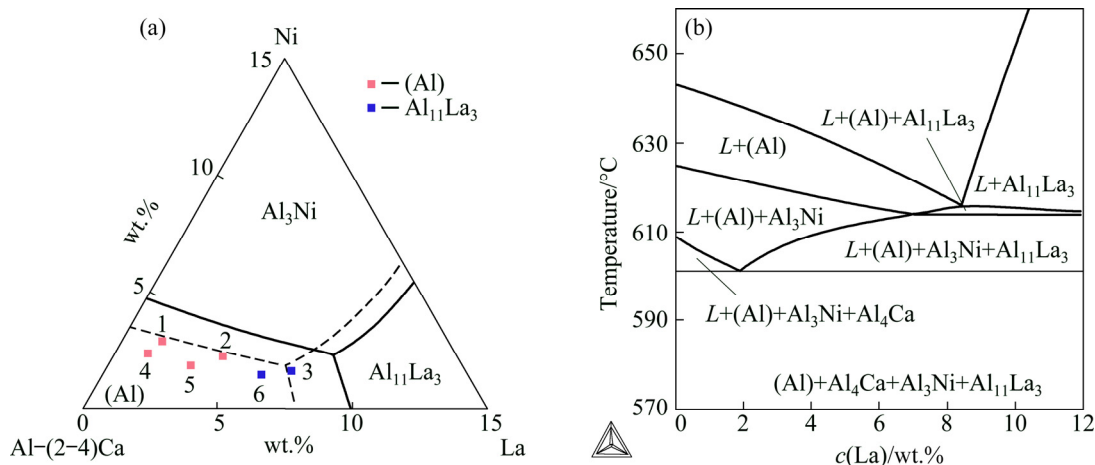


Fig. 1 Liquidus projection of Al–Ca–Ni–La system in aluminum corner (a) and isopleth at 4 wt.% Ca and 2.5 wt.% Ni (b) (The dashed line in Fig. 1(a) indicates the liquidus projection for the system at 4% Ca)

Depending on the actual chemical composition, the structure of hypoeutectic alloys can be formed through binary eutectic reaction either $L \rightarrow (\text{Al}) + \text{Al}_3\text{Ni}$ or $L \rightarrow (\text{Al}) + \text{Al}_{11}\text{La}_3$, followed by a ternary eutectic reaction either $L \rightarrow (\text{Al}) + \text{Al}_3\text{Ni} + \text{Al}_4\text{Ca}$ or $L \rightarrow (\text{Al}) + \text{Al}_{11}\text{La}_3 + \text{Al}_3\text{Ni}$, and the solidification ends via an invariant eutectic reaction $L \rightarrow (\text{Al}) + \text{Al}_{11}\text{La}_3 + \text{Al}_3\text{Ni} + \text{Al}_4\text{Ca}$ at $\sim 601^\circ\text{C}$ (Fig. 1(b)). An increase in the content of Ca leads to a narrowing of the area of the (Al) (see dashed line in Fig. 1(a)). Moreover, analysis of the microstructure of experimental alloys revealed the wider area of primary crystallization of the $\text{Al}_{11}\text{La}_3$ phase

compared to the calculated data (see Figs. 1 and 2). From the analysis of the microstructure, it can also be seen that the ultra-fine eutectic in hypoeutectic alloys with 4 wt.% Ca occupies more than half of the volume (Fig. 2). In accordance with the theoretical analysis (see Table 4), the total volume fraction of the eutectic intermetallics in these alloys can vary in the range of 15–25 vol.%. Due to the low density of the Al_4Ca compound (Table 3), an increase in Ca content leads to a marked increase in the volume fraction of the intermetallic phase (Table 4). At the same time, we can observe a significant decrease in the alloys density (Table 4).

Table 3 Characteristics of phases in Al-rich corner of Al–Ca–Ni–La system [36,37]

Formula	Composition		Crystal lattice	Density/($\text{g}\cdot\text{cm}^{-3}$)	Hardness (HV)
	wt.%	at.%			
Al_4Ca	27Ca	20Ca	Tetr. $I4/mmm$, Pearson symbol: tI10, $a=4.36 \text{ \AA}$; $c=11.09 \text{ \AA}$	2.35	200–260
Al_3Ni	53Ni	25Ni	Orthorhom. $Pnma$, Pearson symbol: oP16, $a=6.61 \text{ \AA}$; $b=7.37 \text{ \AA}$; $c=4.81 \text{ \AA}$	3.95	700–770
$\text{Al}_{11}\text{La}_3$	57La	20La	Orthorhom. $Immm$, Pearson symbol: oI28, $a=4.43 \text{ \AA}$; $b=13.14 \text{ \AA}$; $c=10.13 \text{ \AA}$	4.01	400
Al_9CaNi	12Ca, 17Ni	9Ca, 9Ni	Hex. $P63/mmc$, Pearson symbol: hP22, $a=7.60 \text{ \AA}$; $c=7.94 \text{ \AA}$	2.85	–

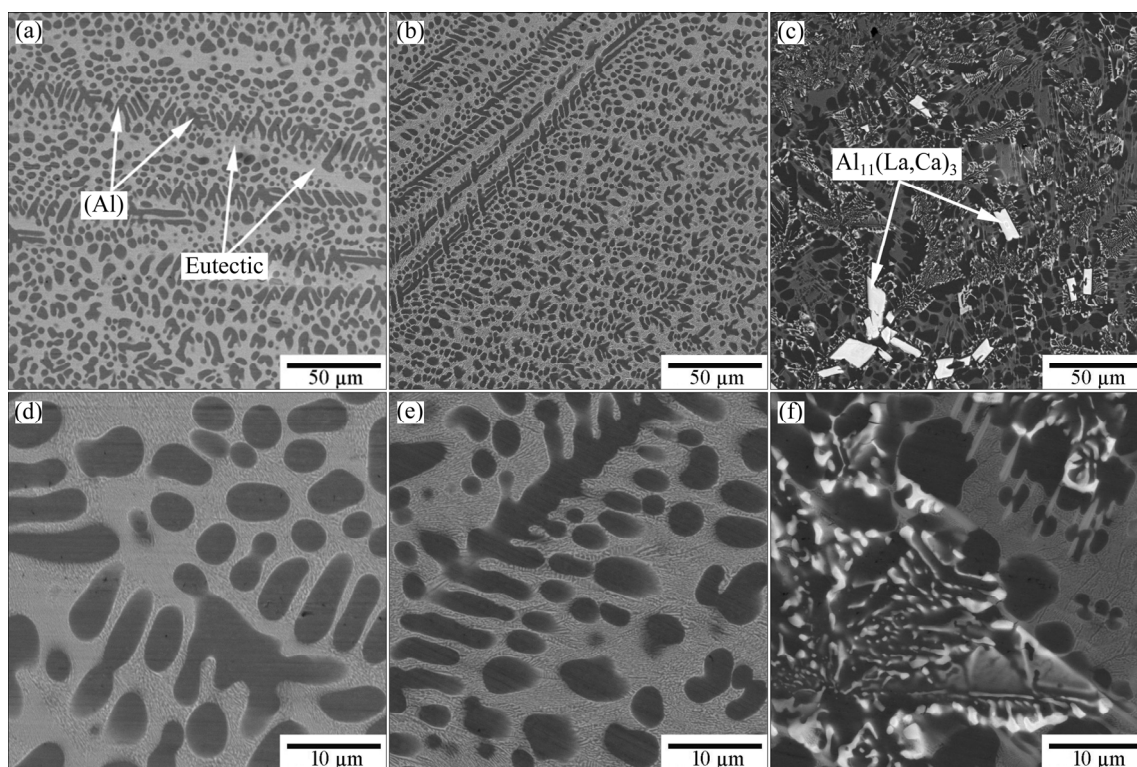


Fig. 2 SEM images showing as-cast microstructure of experimental alloys from Table 1 (obtained at regular melt cooling rates of about 10 K/min): (a, d) No. 4; (b, e) No. 5; (c, f) No. 6

Table 4 Fractions of eutectic intermetallic phases in hypoeutectic alloys and their theoretical density

No.	Chemical composition of alloy/wt.% (at.%)				Fraction of intermetallics/wt.% (vol.%)			Total fraction/wt.% (vol.%)	Calculated density/(g·cm ⁻³)
	Al	Ca	Ni	La	Al ₄ Ca	Al ₃ Ni	Al ₁₁ La ₃		
1	Bal.	2 (1.3)	4 (1.8)	1 (0.2)	5.65 (6.8)	9.45 (6.6)	1.66 (1.2)	16.76 (14.6)	2.77
2	Bal.	2 (1.4)	3 (1.4)	3 (0.6)	5.67 (6.9)	7.10 (5.0)	5.10 (3.8)	17.87 (15.7)	2.78
3	Bal.	2 (1.4)	2 (0.9)	5 (1.0)	5.69 (6.9)	4.70 (3.3)	8.51 (6.4)	18.90 (16.6)	2.80
4	Bal.	4 (2.7)	3 (1.4)	1 (0.2)	13.14 (15.5)	7.10 (4.9)	1.66 (1.2)	21.9 (21.6)	2.71
5	Bal.	4 (2.7)	2.5 (1.2)	3 (0.6)	13.18 (15.7)	5.89 (4.1)	5.10 (3.8)	24.17 (23.6)	2.74
6	Bal.	4 (2.8)	1.5 (0.7)	5 (1.0)	13.20 (15.7)	3.51 (2.4)	8.51 (6.3)	25.22 (24.4)	2.75

Indeed, the density of the Al₄Ca₃Ni₁La alloy, totally containing 4 wt.% of heavy Ni and La, is close to that of pure aluminum. However, due to inconsistencies between the calculated and experimental data on the phase regions described above, a more detailed experimental analysis of the quaternary system is necessary for accurate determination of the phase equilibria in this system.

For a more detailed analysis of the quaternary system, additional studies of the microstructure of alloys (Nos. 4 and 5 in Table 1) obtained during slow solidification (melt cooling rate is ~0.01 K/min) and after prolonged high-temperature annealing of the as-cast specimens analyzed above (presented in Fig. 2) were carried out. In both cases, we can expect the formation of the phase composition close to the equilibrium one. According to EMPA, the microstructure of alloy No. 4 (Fig. 3(a)) contains two eutectic phases: predicted binary Al₄Ca and ternary compound with the formula close to Al₉CaNi. Lanthanum distributes among these compounds and does not form the Al₁₁La₃ phase. An increase in the content of La in alloy No. 5 (Fig. 3(b)) leads to the appearance of relatively coarse bright crystals of the Al₁₁La₃ phase. The chemical compositions of the phases as determined by EMPA are presented in Table 5. The data suggest a significant mutual solubility between the binary Al₁₁La₃ and Al₄Ca compounds. The Ca and La atoms in the lattice interchange with each other in the equivalent positions. XRD analysis (Fig. 4) of the as-annealed samples (Figs. 3(c, d)) well confirms the results obtained by EMPA. Table 5 gives experimental data on the quantitative parameters of the phases, in particular, their fraction, crystal lattice parameters and densities calculated based on these data. It can be seen that both alloys consist of the Al₄Ca and

Al₉CaNi phases, the total volume fraction of which is about 30%. Due to the high content of La, alloy No. 5 also contains a small amount of the Al₁₁La₃ phase. However, the main amount of La is dissolved in the Al₄Ca phase. As can be seen, an increase in the content of La in Al₄Ca leads to a marked increase in the *a* lattice parameter and density. Indeed, according to Table 3, the natural density of Al₄Ca is about 2.35 g/cm³ while replacing 10% of calcium atoms by lanthanum (see Table 5) leads to an increase in the density of the compound to 2.49 g/cm³, i.e., by 8%. Replacing more than 20% calcium atoms increases the density by 13% (Table 6). Noticeable changes in the lattice parameter and density can also be observed for the Al₁₁La₃ compound. Replacing more than 32% of the lanthanum atoms by calcium leads to a decrease in the density of the compound to 3.51 g/cm³. It should be emphasized that the ternary Al–Ca–La system was not previously analyzed and therefore additional studies of the ternary system are required for a more detailed analysis of the observed mutual solubility. Analysis of the properties of the Al₉CaNi compound revealed a certain increase of its density, which is associated with the dissolution of a relatively small amount of lanthanum. An additional increase in the content of lanthanum (see data for alloy No. 5 in Table 6) leads to a certain increase in the *c* parameter of the crystal lattice, while the density remains almost unchanged. This result is due to a slight increase of the lanthanum content, the presence of which leads to stretching (i.e., increase in the volume) of the crystal lattice.

Thus, based on the analysis above, three phases Al₄(Ca,La), Al₁₁(La,Ca)₃ and Al₉CaNi are in equilibrium with (Al) in the Al–Ca alloys. Taking into account the structure of the ternary Al–Ca–Ni system [23], the projection of the liquidus surface

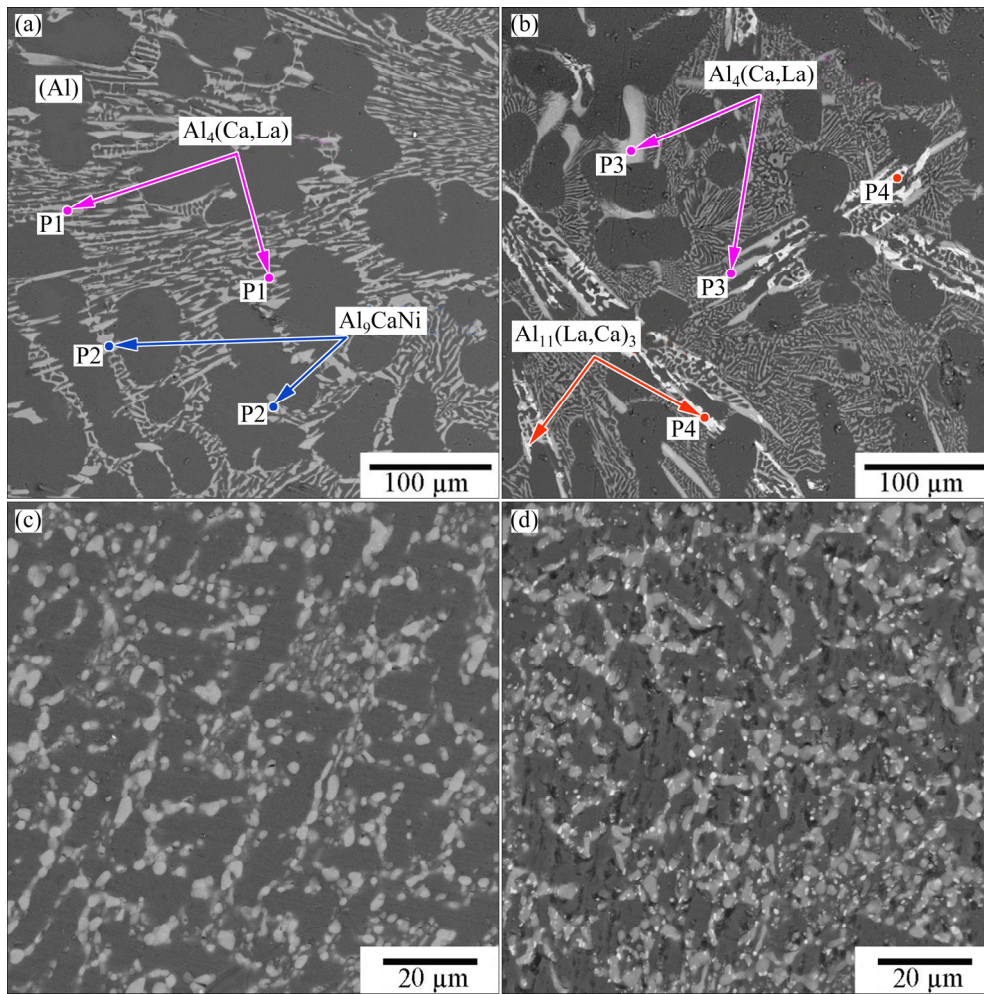


Fig. 3 SEM images showing microstructure of alloys No. 4 (a, c) and No. 5 (b, d) obtained during slow solidification at melt cooling rate of about 0.01 K/min (a, b) and after prolonged high-temperature annealing (at 500 °C for 10 h) of as-cast samples obtained at regular cooling rate of 10 K/s (c, d)

Table 5 Chemical compositions of phases in Al–Ca–Ni–La alloys determined by EMPA

Point in Figs. 3(a, b)	Chemical composition/at.%				Identified phase
	Al	Ca	Ni	La	
P1	Bal.	17.52±0.18	–	1.92±0.24	Al ₄ (Ca,La)
P2	Bal.	8.59±0.13	9.10±0.25	0.51±0.18	Al ₉ CaNi
P3	Bal.	15.76±0.17	–	4.25±0.28	Al ₄ (Ca,La)
P4	Bal.	6.45±0.13	–	14.3±0.28	Al ₁₁ (La,Ca) ₃

of the quaternary system (Fig. 5(a)) was proposed. In accordance with it, two invariant reactions can be expected near the aluminum corner: peritectic $L + Al_3Ni \rightarrow Al_9CaNi + Al_{11}(La,Ca)_3$ (P) and eutectic $L \rightarrow Al + Al_4(Ca,La) + Al_9CaNi + Al_{11}(La,Ca)_3$ (E) which, according to the results of DSC, takes place at ~603 °C. Accordingly, the expected solid state phase-field distribution is proposed in Fig. 5(b). As can be seen, the main part of the diagram consists

of two four-phase areas: (Al) + Al₄(Ca,La) + Al₁₁(La,Ca)₃ + Al₉CaNi and (Al) + Al₄(Ca,La) + Al₁₁(La,Ca)₃ + Al₃Ni (marked as 1 and 2) and two three-phase areas: (Al) + Al₁₁(La,Ca)₃ + Al₉CaNi and (Al) + Al₄(Ca,La) + Al₉CaNi (marked as 3 and 4). The Al₄(Ca,La) phase is not in equilibrium with the Al₃Ni phase and therefore the hypoeutectic quaternary alloys always contain the ternary Al₉CaNi phase. Due to the relatively high solubility

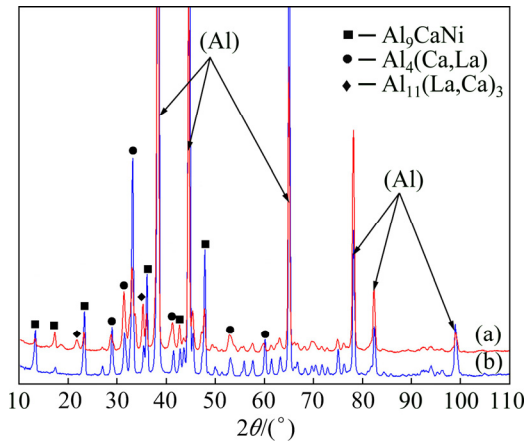


Fig. 4 XRD patterns of Al₄Ca₃La₃Ni (a) and Al₄Ca₁La₃Ni (b) alloys

of La in Al₄(Ca,La) phase, the four-phase area is sufficiently narrow and therefore the vast majority of the hypoeutectic alloy composites corresponds to the (Al) + Al₄(Ca,La) + Al₉CaNi three-phase area.

3.2 Analysis of Al–Ca–Ni–La system base hypoeutectic alloy

As can be seen from Fig. 2, hypoeutectic alloys Nos. 4 and 5 at 4 wt.% Ca have an ultra-fine

eutectic structure which is beneficial for obtaining high mechanical properties. On the other hand, an additional increase in strength can be achieved by alloying with small amounts of zirconium and scandium. The microstructure of the new alloy Al₄Ca_{2.5}Ni₃La_{0.2}Zr_{0.1}Sc (No. 7) with zirconium and scandium additives in the as-cast state is shown in Fig. 6. As can be seen, no new structural components are detected compared with Fig. 2. The fine eutectic layers which were liquid during casting separate the (Al) solid grains from each other and also locate in the grain boundary triple junctions (Figs. 6(a, b)). TEM analysis reveals that the eutectic particles are slightly elongated (in the direction of heat removal in alloy solidification) and have a size of about 100–150 nm in the transverse direction and about 150–250 nm in the longitudinal direction (Figs. 6(c, d)). EMPA shows that zirconium and scandium distribute between the aluminum solid solution (Al) and the eutectic (Table 7). To confirm the possibility of alloy hardening, stepwise annealing of the alloy according to the mode in Table 2 was conducted. The Vickers hardness was measured after each step. The results are shown in Fig. 7. For the steps

Table 6 Fractions of eutectic intermetallic phases and their lattice parameters and densities calculated based on XRD data

Phase	Pearson symbol	Alloy	Volume fraction/%	Lattice parameter/Å	Phase density/(g·cm ⁻³)
(Al)	cF4	Al ₄ Ca ₃ La ₃ Ni	69.9	<i>a</i> =4.05	2.7
		Al ₄ Ca ₁ La ₃ Ni	72.3	<i>a</i> =4.05	2.7
Al ₉ CaNi	hP22	Al ₄ Ca ₃ La ₃ Ni	15.6	<i>a</i> =7.58, <i>c</i> =7.93	2.88
		Al ₄ Ca ₁ La ₃ Ni	15.4	<i>a</i> =7.58, <i>c</i> =7.89	2.89
Al ₁₁ (La, Ca) ₃	oI28	Al ₄ Ca ₃ La ₃ Ni	1.7	<i>a</i> =4.42, <i>b</i> =13.06, <i>c</i> =10.15	3.51
Al ₄ (Ca, La)	tI10	Al ₄ Ca ₃ La ₃ Ni	12.8	<i>a</i> =4.36, <i>c</i> =11.19	2.6
		Al ₄ Ca ₁ La ₃ Ni	12.3	<i>a</i> =4.34, <i>c</i> =11.20	2.49

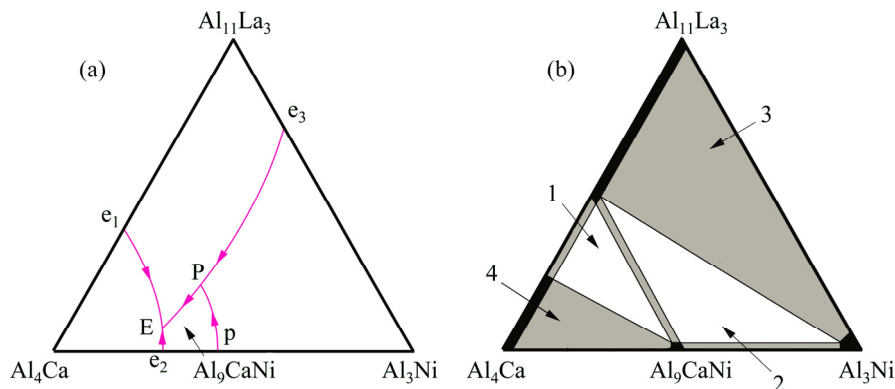


Fig. 5 Proposed phase diagrams of Al–Ca–Ni–La system: (a) Polythermal projection; (b) Solid state phase-field distribution

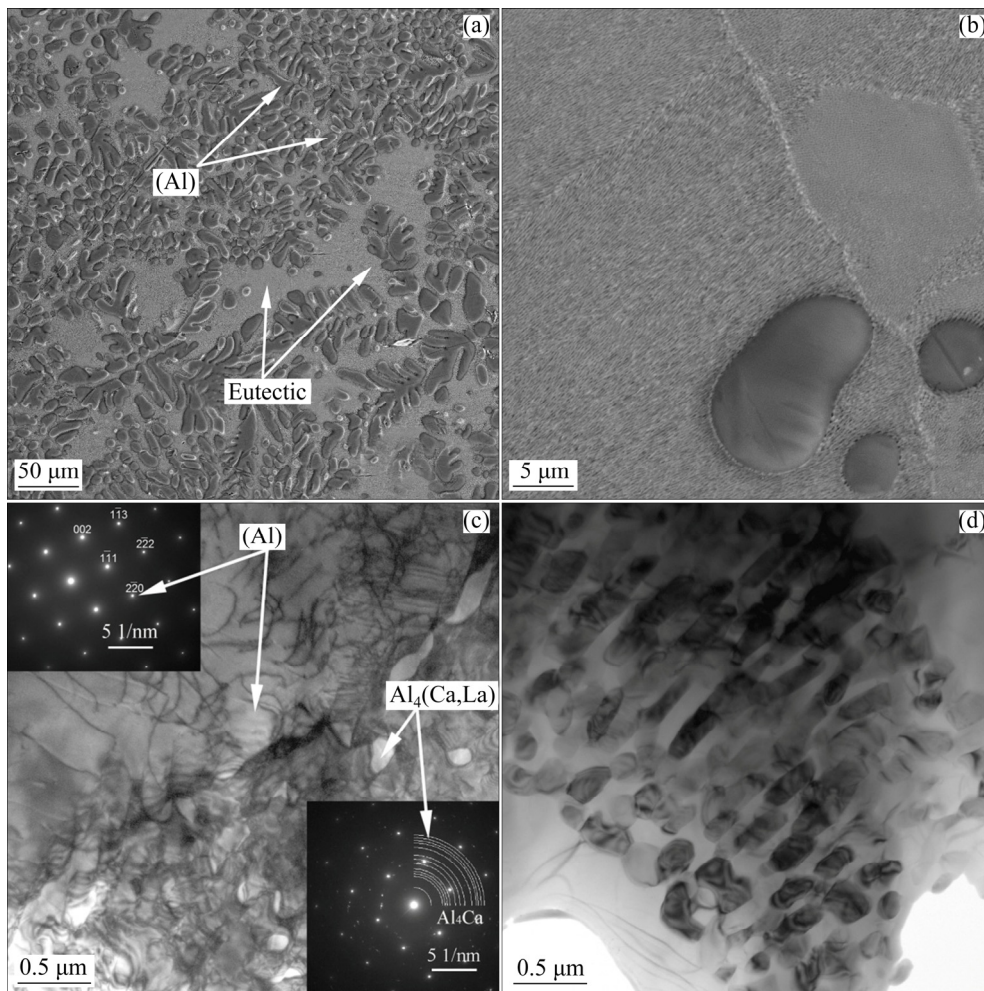


Fig. 6 SEM (a, b) and TEM (c, d) images showing microstructure of experimental $\text{Al}_4\text{Ca}_{2.5}\text{Ni}_3\text{La}_{0.2}\text{Zr}_{0.1}\text{Sc}$ alloy: (a, c) General view; (b, d) Eutectic structure

Table 7 Chemical compositions of structural components in $\text{Al}_4\text{Ca}_{2.5}\text{Ni}_3\text{La}_{0.2}\text{Zr}_{0.1}\text{Sc}$ alloy

Structural component	Chemical composition/at.%					
	Al	Ca	Ni	La	Zr	Sc
(Al)	Bal.	–	–	–	0.39 ± 0.23	0.12 ± 0.07
Eutectic	Bal.	5.19 ± 0.11	3.61 ± 0.17	4.14 ± 0.21	0.22 ± 0.23	0.12 ± 0.08

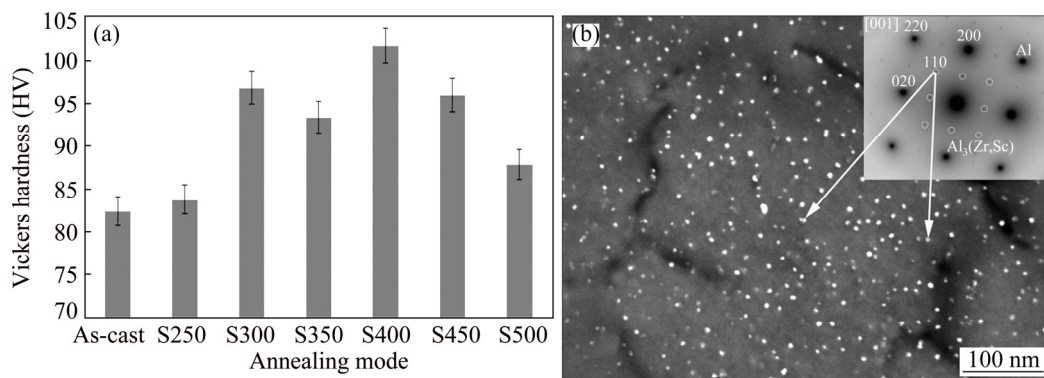


Fig. 7 Effect of stepwise annealing on Vickers hardness of $\text{Al}_4\text{Ca}_{2.5}\text{Ni}_3\text{La}_{0.2}\text{Zr}_{0.1}\text{Sc}$ alloy (a) and TEM image showing precipitates of $\text{Al}_3(\text{Zr,Sc})\text{-L}_{12}$ phase forming during annealing (b)

S300 and S400, we can observe a substantial hardening by ~25% compared to the as-cast state. In accordance with the TEM results (Fig. 7), this hardening is caused by the formation of nanoparticles of the L1₂ type phase (Al₃(Zr,Sc)) with a diameter of about 10–15 nm.

According to uniaxial tensile tests (Table 8), the base alloy in the as-cast state has an average strength that is comparable to that of industrial cast aluminum alloy A356 [38] after quenching and artificial aging. The addition of zirconium and scandium significantly increases the strength of the alloy while maintaining an acceptable elongation.

4 Discussion

Due to the high volume fraction of eutectic intermetallic compounds, new Al–Ca–Ni–La hypoeutectic alloys have many advantages in comparison with branded Al–Si cast alloys. First of all, the strength of the as-cast new alloys (Table 8) is comparable to those of branded Al–Si alloys after artificial aging. In addition, new alloys, unlike Al–Si branded ones, can be strengthened by small additions of zirconium and scandium (Fig. 7(a)). A simple calculation shows that the dissolution of 0.2 wt.% Zr and 0.1 wt.% Sc in (Al) should lead to the formation of about 0.4 vol.% of the L1₂-type phase. Taking into account that the average diameter (D_S) of the precipitates is about 15 nm, the interprecipitate spacing λ can be calculated using well known relationship [39]:

$$\lambda = 0.5D_S \cdot \left(\sqrt{\frac{2\pi}{3f_v}} - \frac{\pi}{4} \right) \quad (1)$$

where f_v is the particle volume fraction. According to Eq. (1), λ is about 165 nm. The modified Orowan model for spherical unsharable precipitates [40] can be used for analyzing the increase in yield strength associated with the nanoparticles. According to this model,

$$\Delta\sigma_{0.2}(L1_2) = \frac{0.4Mgb}{\pi\sqrt{(1-\nu)}} \cdot \frac{\ln(2\bar{R}/r_0)}{\lambda} \quad (2)$$

where M is the Taylor factor varying in 2.44–3.7 range, G and b are the shear modulus and the absolute value of Burgers vector of Al, respectively, \bar{R} is the average radius of circular cross-section, ν is Poisson's ratio of Al and $r_0=1.5b$. Thus, if the average Taylor factor is 3.1, the increase in the yield strength of the aluminum matrix caused by the Al₃(Zr,Sc) nanoparticles is about 73 MPa.

As can be seen from Table 8, the fine eutectic structure also contributes significantly to the strengthening. However, it will not be entirely correct to perform a similar calculation for the eutectic particles since they have an elongated shape. If we assume that the particles have a shape close to ellipsoid, Eq. (2) can be modified as follows:

$$\Delta\sigma_{0.2}(e) = \frac{0.4Mgb}{\pi\sqrt{(1-\nu)}} \cdot \frac{\ln[2P_e / (\pi r_0)]}{\lambda} \quad (3)$$

where P_e is the ellipse perimeter. According to quantitative metallographic analysis, λ for eutectic particles is 150 nm. If we also assume that the particles have an average length of 200 nm and a width of 150 nm, the increase in the yield strength (according to Eq. (3)) caused by the eutectic particles is 160 MPa. Additionally, we should also take into account that the aluminum phase in the eutectic is also reinforced by the L1₂ nanoparticles.

To calculate the resulting strength of the alloy, we can use the basic additivity principle for the composite properties. Based on it, the yield strength of the alloy can be calculated using simple equation:

$$\sigma_{0.2} = V_{(Al)}(\sigma_{0.2}(Al) + \Delta\sigma_{0.2}(L1_2)) + V_e((\sigma_{0.2}(Al) + \Delta\sigma_{0.2}(L1_2)) + \Delta\sigma_{0.2}(e)) \quad (4)$$

where $\sigma_{0.2}(Al)$ is the yield strength of pure aluminum (can be accepted at ~30 MPa) and $V_{(Al)}$ and V_e are the volume fractions of aluminum and eutectic, respectively. In accordance with quantitative metallographic analysis, the fraction of the eutectic is about 60 vol.% (Fig. 6(a)). Thus, the yield strength is about 130 MPa for the base alloy and 200 MPa for the alloy with small additives of

Table 8 Mechanical properties after uniaxial tensile tests of alloys

Alloy	UTS/MPa		YS/MPa		$\delta/\%$	
	Measured	Average	Measured	Average	Measured	Average
Al4Ca2.5Ni3La	196, 195, 195, 194	195	141, 142, 141, 140	141	2.6, 2.2, 2.3, 2.5	2.4
Al4Ca2.5Ni3La0.2Zr0.1Sc	299, 301, 305, 287	298	193, 198, 195, 192	194	1.5, 2.4, 1.9, 2.0	2.0

Zr and Sc. The calculated result is quite close to the experimental data and can be used for estimating the yield strength of the eutectic composite alloys.

Another interesting feature of these alloys is their relatively low density due to calcium content. As can be seen from Table 3, the density of the Al_4Ca phase is lower than that of pure aluminum. Dissolving La in Al_4Ca increases its density up to 2.6 g/cm^3 , but it still remains lower than that of pure aluminum. The ternary Al_9CaNi compound has a density of 2.85 g/cm^3 , which is slightly higher than that of aluminum but significantly lower than that of the binary Al_3Ni compound (3.95 g/cm^3). Taking into account the volume fraction and actual density of the phases (Table 6), the calculated density of the $\text{Al}_4\text{Ca}_1\text{La}_2.5\text{Ni}$ and $\text{Al}_4\text{Ca}_3\text{La}_2.5\text{Ni}$ alloys is 2.70 and 2.73 g/cm^3 , respectively, which is in a good agreement with the experimental data (2.69 and 2.72 g/cm^3). As can be seen, even at 3 wt.% La, the density of the alloy barely exceeds the density of pure aluminum, despite the total volume fraction of intermetallic compounds in the structure is more than 30 vol. % (Table 6). It should be noted that despite the calculation in the Thermo-Calc program does not provide a correct analysis of the phase composition, the obtained calculated data can nevertheless be used for estimating the density of the alloys (see Table 4). The obtained result is explained, on the one hand, by an increase in the density (see Table 4) of the Al_4Ca compound (as a result of the dissolution of La), and on the other hand, by the compensation of the lower density of the ternary Al_9CaNi compound (compared with the Al_3Ni compound) at the expense of its higher volume fraction, which leads to a decrease in the volume fraction of aluminum with a lower density.

Another advantage of the new alloys is their relatively high thermal stability which is associated with a high volume fraction of intermetallic phases. Indeed, as can be seen from Fig. 8, during heating in the range of $50\text{--}600 \text{ }^\circ\text{C}$, the coefficient of thermal expansion (CTE) of the new alloy varies slightly in the range of $(22.5\text{--}24)\times 10^{-6} \text{ K}^{-1}$. In contrast, the CTE of the branded A356 alloy increases significantly in the temperature range of $200\text{--}300 \text{ }^\circ\text{C}$, reaching a maximum value of more than $27\times 10^{-6} \text{ K}^{-1}$. The thermal stability of the mechanical properties can be evaluated by analyzing the microstructure and microhardness after prolonged high-temperature annealing. After

annealing at $450 \text{ }^\circ\text{C}$ for 12 h, we can observe coarsening of the eutectic structure; however, the intermetallic particles are still less than $1 \mu\text{m}$ in diameter (see Fig. 9). The microhardness of the

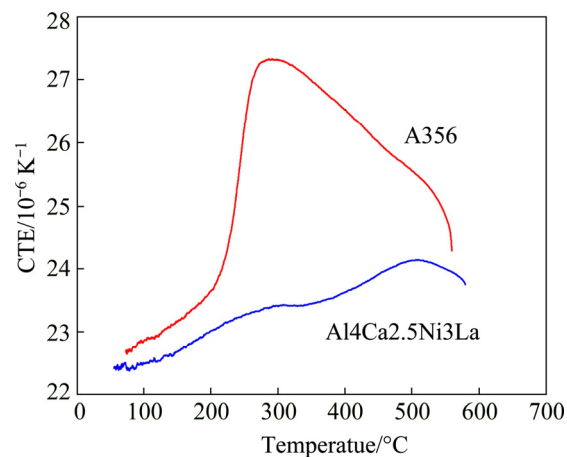


Fig. 8 Coefficient of thermal expansion (CTE) versus temperature for $\text{Al}_4\text{Ca}_2.5\text{Ni}_3\text{La}$ and A356 alloys

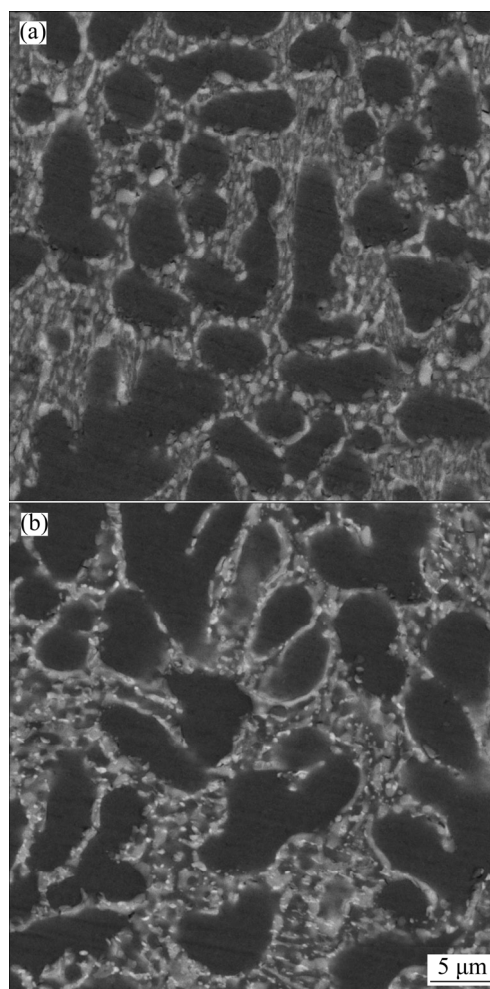


Fig. 9 Microstructures of alloys No. 4 (a) and No. 5 (b) after prolonged high-temperature annealing at $450 \text{ }^\circ\text{C}$ for 10 h

Al₄Ca₃La_{2.5}Ni alloy is still high enough after annealing and decreases from HV 82 to 60, i.e., by 27%. It should be noted that the microhardness of the alloy with small additives of Zr and Sc, even after annealing at 500 °C (Fig. 7), remains higher than HV 85, which is directly related to the influence of the L₁₂ nanoparticles.

Thus, new hypoeutectic alloys based on the quaternary Al–Ca–Ni–La system have low density, high dispersion of the eutectic in the as-cast state, can be significantly strengthened by small additions of Zr and Sc, and have a low coefficient of thermal expansion and high thermal stability of the structure and properties. Due to these advantages, the new Al–Ca–Ni–La system base alloys can be considered as a promising replacement for the branded Al–Si alloys for the manufacture of critical products.

5 Conclusions

(1) Phase equilibria in the quaternary Al–Ca–Ni–La system near the aluminum corner have been analyzed using computational and experimental analysis. EMPA and XRD analyses have revealed significant mutual solubility between the binary Al₄Ca (Al₄(Ca,La)) and Al₁₁La₃ (Al₁₁(La,Ca)₃) compounds (Ca and La atoms interchange in the equivalent positions of the crystal lattice), which leads to changes in their lattice parameters and densities. The binary Al₄(Ca,La) and Al₁₁(La,Ca)₃ and the ternary Al₉CaNi compounds are in equilibrium with the aluminum solid solution (Al) in promising Al–Ca hypoeutectic alloys. The revealed phase equilibria imply the presence of two invariant transformations: peritectic $L + Al_3Ni \rightarrow Al_9CaNi + Al_{11}(La,Ca)_3$ and eutectic $L \rightarrow Al_4(Ca,La) + Al_9CaNi + Al_{11}(La,Ca)_3$ in the considered part of the system.

(2) The alloys of 2–4 wt.% Ca, 2–4 wt.% Ni and 1–3 wt.% La ranges have an ultra-fine hypoeutectic structure with an about 30 vol.% total volume fraction of eutectic intermetallics which allows one to classify these alloys as natural Al-matrix composites. The ultra-fine eutectic structure (the eutectic particles have a size of about 100–150 nm in the transverse direction and 150–250 nm in the longitudinal direction) produces significant strengthening, the magnitude of which can be well described using the modified Orowan

looping mechanism model.

(3) The alloys can undergo additional strengthening (by ~25%) due to the introduction of small additives of Zr and Sc (0.2 and 0.1 wt.%, respectively). In accordance with TEM data, this result is associated with the decomposition of the aluminum solution (Al) and simultaneous formation of nanoparticles (the average diameter is about 10–15 nm) of the L₁₂ (Al₃(Zr,Sc)) phase during annealing of the alloy at 350–400 °C.

(4) Due to the high volume fraction of eutectic intermetallic phases, the new alloys have low coefficients of thermal expansion and high thermal stability of the structure and mechanical properties. Taking into account the advantages described above, the new Al–Ca–Ni–La base alloys can be considered as a promising replacement for the branded Al–Si alloys in the manufacture of critical parts.

Acknowledgments

The study was carried out by the financial support of the grant of the Russian Science Foundation (Project No. 18-79-00345) (preparation of alloys, electron microscopy (SEM, EMPA, TEM), tensile tests) and by the Ministry of Science and Higher Education of the Russian Federation in the framework of Increase Competitiveness Program of MISiS (No. P02-2017-2-10) (thermodynamic calculations, dilatometry, DSC and XRD).

References

- [1] CAO Zu-jun, KONG Gang, CHE Chun-shan, WANG Yan-qi, PENG Hao-tang. Experimental investigation of eutectic point in Al-rich Al–La, Al–Ce, Al–Pr and Al–Nd systems [J]. *Journal of Rare Earths*, 2017, 35(10): 1022–1028.
- [2] AMARAL J C B S, SÁ M L C G, MORAIS C A. Recovery of uranium, thorium and rare earth from industrial residues [J]. *Hydrometallurgy*, 2018, 181: 148–155.
- [3] SONG Xian-chen, YAN Hong, ZHANG Xiao-jun. Microstructure and mechanical properties of Al–7Si–0.7Mg alloy formed with an addition of (Pr+Ce) [J]. *Journal of Rare Earths*, 2017, 35(4): 412–418.
- [4] LIN Gao-yong, LI Kun, FENG Di, FENG Yong-ping, SONG Wei-yuan, XIAO Meng-qiong. Effects of La–Ce addition on microstructure and mechanical properties of Al–18Si–4Cu–0.5Mg alloy [J]. *Transactions of Nonferrous Metals Society of China*, 2019, 29(8): 1592–1600.
- [5] LI Diao-feng, CUI Chun-xiang, WANG Xin, WANG Qing-zhou, CHEN Cheng, LIU Shui-qing. Microstructure evolution and enhanced mechanical properties of eutectic Al–Si die cast alloy by combined alloying Mg and La [J].

- Materials and Design, 2016, 90: 820–828.
- [6] LIAO Heng-cheng, HU Yi-yun. Effect of RE addition on solidification process and high-temperature strength of Al–12%Si–4%Cu–1.6%Mn heat-resistant alloy [J]. Transactions of Nonferrous Metals Society of China, 2019, 29(6): 1117–1126.
- [7] JIANG Wen-ming, FAN Zi-tian, DAI Yu-cheng, LI Chi. Effects of rare earth elements addition on microstructures, tensile properties and fractography of A357 alloy [J]. Materials Science and Engineering A, 2014, 597: 237–244.
- [8] SIMS Z C, WEISS D, McCALL S K, McGUIRE M A, OTT R T, GEER T, RIOS O, TURCHI P A E. Cerium-based, intermetallic-strengthened aluminum casting alloy: High-volume co-product development [J]. JOM, 2016, 68: 1940–1947.
- [9] SIMS Z C, RIOS O, McCALL S K, van BUUREN T, OTT R T. Characterization of near net-shape castable rare earth modified aluminum alloys for high temperature application [C]/WILLIAMS E. Light Metals 2016. Springer, Cham, 2016.
- [10] SIMS Z C, RIOS O, TURCHI P E A, PERRON A, LEE J R I, LI T T, HAMMONS J A, BAGGE-HANSEN M, WILLEY T M, AN K, CHEN Y, KING A H, McCALL S C. High performance aluminum–cerium alloys for high-temperature applications [J]. Materials Horizons, 2017, 4: 1070–1078.
- [11] WEISS D, RIOS O, SIMS Z C, McCALL S K, OTT R T. Casting characteristics of high cerium content aluminum alloys [C]/RATVIK A. Light Metals 2017. The Minerals, Metals & Materials Series. Springer, Cham, 2017.
- [12] HE Yang, LIU Jian-hua, QIU Sheng-tao, DENG Zhen-qiang, ZHANG Jie, SHEN Yao-zu. Microstructure evolution and mechanical properties of Al–La alloys with varying La contents [J]. Materials Science and Engineering A, 2017, 701: 134–142.
- [13] MANCA D R, CHURYUMOV A Y, POZDNIAKOV A, PROSVIRYAKOV A, RYABOV D, KROKHIN A, KOROLEV V, DAUBARAYTE D. Microstructure and properties of novel heat resistant Al–Ce–Cu alloy for additive manufacturing [J]. Metals and Materials International, 2019, 25(3): 633–640.
- [14] COURY F G, KIMINAMI C S, BOTTA W J, BOLFARINI C, KAUFMANA M J. Design and production of Al–Mn–Ce alloys with tailored properties [J]. Material and Design, 2016, 110: 436–448.
- [15] AKOPYAN T K, BELOV N A, NAUMOVA E A, LETYAGIN N V. New in-situ Al matrix composites based on Al–Ni–La eutectic [J]. Materials Letters, 2019, 245: 110–113.
- [16] BELOV N A, NAUMOVA E A, ALABIN A N, MATVEEVA I A. Effect of scandium on structure and hardening of Al–Ca eutectic alloys [J]. Journal of Alloys and Compounds, 2015, 646: 741–747.
- [17] TIAN L, KIM H, ANDERSON I, RUSSELL A. The microstructure-strength relationship in a deformation processed Al–Ca composite [J]. Materials Science and Engineering A, 2013, 570: 106–113.
- [18] BELOV N A, NAUMOVA E A, DOROSHENKO V V, AVXENTIEVA N N. Combined effect of calcium and silicon on the phase composition and structure of Al–10%Mg Alloy [J]. Russian Journal of Non-Ferrous Metals, 2018, 59(1): 67–75.
- [19] BELOV N A, NAUMOVA E A, AKOPYAN T K, DOROSHENKO V V. Design of multicomponent aluminium alloy containing 2 wt% Ca and 0.1 wt% Sc for cast products [J]. Journal of Alloys and Compounds, 2018, 762: 528–536.
- [20] CHAUBEY A K, SCUDINO S, MUKHOPADHYAY N K, KHOSHKHOO M S, MISHRAC B K, ECKERTA J. Effect of particle dispersion on the mechanical behavior of Al-based metal matrix composites reinforced with nanocrystalline Al–Ca intermetallics [J]. Journal of Alloys and Compounds, 2012, 536: 134–137.
- [21] JIANG Yu-rong, SHI Xi, BAO Xiao-heng, HE Ye, HUANG Shuai-xiong, WU Di, BAI Wei-min, LIU Li-bin, ZHANG Li-gang. Experimental investigation and thermodynamic assessment of Al–Ca–Ni ternary system [J]. Journal of Materials Science, 2017, 52(20): 12409–12426.
- [22] SUWANPREECHA C, PANDEE P, PATAKHAM U, LIMMANEEVICHITR C. New generation of eutectic Al–Ni casting alloys for elevated temperature services [J]. Materials Science and Engineering A, 2018, 709: 46–54.
- [23] BELOV N A, ALABIN A N, MATVEEVA I A, ESKIN D G. Effect of Zr additions and annealing temperature on electrical conductivity and hardness of hot rolled Al sheets [J]. Transactions of Nonferrous Metals Society of China, 2015, 25(9): 2817–2826.
- [24] BELOV N A, NAUMOVA E A, ESKIN D G. Casting alloys of the Al–Ce–Ni system: Microstructural approach to alloy design [J]. Materials Science and Engineering A, 1999, 271: 134–142.
- [25] BELOV N A, NAUMOVA E A, ALABIN A N, MATVEEVA I A. Effect of scandium on structure and hardening of Al–Ca eutectic alloys [J]. Journal of Alloys and Compounds, 2015, 646: 741–747.
- [26] TOROPOVA L S, ESKIN D G, KHARAKTEROVA M L, DOBATKINA T V. Advanced aluminum alloys containing scandium: structure and properties [M]. Amsterdam: Gordon and Breach Science Publishers, 1998.
- [27] JIA Zhi-hong, RØYSET J, SOLBERG J K, LIU Qing. Formation of precipitates and recrystallization resistance in AlScZr alloys [J]. Transactions of Nonferrous Metals Society of China, 2012, 22(8): 1866–1871.
- [28] ZHOU W W, CAI B, LI W J, LIU Z X, YANG S. Heat resistant Al–0.2Sc–0.04Zr electrical conductor [J]. Materials Science and Engineering A, 2012, 552: 353–358.
- [29] BOOTH-MORRISON C, MAO Z, DIAZ M, DUNAND D C, WOLVERTON C, SEIDMAN D N. Role of silicon in accelerating the nucleation of Al₃(Sc,Zr) precipitates in dilute Al–Sc–Zr alloys [J]. Acta Materialia, 2012, 60(12): 4740–4752.
- [30] MARQUIS E A, SEIDMAN D N. Nanoscale structural evolution of Al₃Sc precipitates in Al (Sc) alloys [J]. Acta Materialia, 2001, 49: 1909–1919.
- [31] GUAN Ren-guo, JIN Hong-mei, JIANG Wen-sen, WANG Xiang, WANG Yu-xiang, LI Zheng, ZHANG Jian, LIU Hui-nan. Quantitative contributions of solution atoms, precipitates and deformation to microstructures and properties of Al–Sc–Zr alloys [J]. Transactions of Nonferrous Metals Society of China, 2019, 29(5): 907–918.

- [32] FULLER C B, SEIDMAN D N. Temporal evolution of the nanostructure of Al(Sc, Zr) alloys: Part II—Coarsening of $Al_3(Sc_{1-x}Zr_x)$ precipitates [J]. *Acta Materialia*, 2005, 53: 5415–5428.
- [33] KNIPLING K E, KARNESKY R A, LEE C P, DUNAND D C, SEIDMAN D N. Precipitation evolution in Al–0.1Sc, Al–0.1Zr and Al–0.1Sc–0.1Zr (at.%) alloys during isochronal ageing [J]. *Acta Materialia*, 2010; 58: 5184–5195.
- [34] SHELEKHOV E V, SVIRIDOVA T A. Programs for X-ray analysis of polycrystals [J]. *Metal Science and Heat Treatment*, 2000, 42: 309–313.
- [35] Information on www.thermocalc.com. [EB/OL]. 2019–03–30.
- [36] MONDOLFO L F. Aluminium alloys: Structure and properties [M]. London: Butterworths, 1976.
- [37] MANYAKO M B, ZARECHNYUK O S, YANSON T I. Crystal structure of CaNiAl₉ [J]. *Soviet Physics Crystallography* (translated from *Kristallografiya*), 1987, 32: 816–817.
- [38] POLMEAR I J. Light metals: From traditional alloys to nanocrystals [M]. 4th ed. Oxford, UK: Elsevier, 2006.
- [39] KNIPLING K E, DUNAND D C, SEIDMAN D N. Precipitation evolution in Al–Zr and Al–Zr–Ti alloys during aging at 450–600 °C [J]. *Acta Materialia*, 2008, 56: 1182–1195.
- [40] ZHU A W, STARKE E A. Strengthening effect of unsharable particles of finite size: A computer experimental study [J]. *Acta Materialia*, 1999, 47: 3263–3269.

L₁2 型纳米颗粒增强以 Al–Ca–Ni–La 体系为基体的铝基复合材料

Torgom K. AKOPYAN, Nikolay A. BELOV, Evgeniya A. NAUMOVA,
Nikolay V. LETYAGIN, Tat'yana A. SVIRIDOVA

National University of Science and Technology MISiS, 4 Leninsky pr., Moscow 119049, Russia

摘要: 结合 Thermo-Calc 热模拟程序计算和实验(电子显微镜、微探针分析和 X 射线衍射)研究四元系 Al–(2–4)Ca–Ni–La(质量分数, %)合金在铝角附近的结构。根据得到的相平衡数据, 提出 Al–Ca–Ni–La 体系液相面和固相相场分布的实验投影。显微组织研究表明, 含 2%~4% Ca、2%~4% Ni 和 1%~3%La(质量分数)的合金具有超细的亚共晶组织, 共晶金属间化合物的体积分数为 30%, 因此, 可以将这些合金归类为天然 Al 基复合材料。超细共晶结构产生显著的强化作用, 其机制可以很好地用修订的 Orowan 循环模型描述。在 350~400 °C 退火过程中, 由于 L₁2 型相($Al_3(Zr,Sc)$)纳米颗粒的形成, 添加少量的 Zr 和 Sc(分别为 0.2%和 0.1%, 质量分数)具有显著的强化作用(提高约 25%)。由于共晶金属间化合物的体积分数高, 该新合金具有低的热膨胀系数、高的结构热稳定性和力学性能。

关键词: Al–Ca 合金; 共晶; 金属间化合物; 相图; 稀土元素; 纳米复合材料; 显微组织; 力学性能

(Edited by Bing YANG)